Confocal light sheet microscopy: micron-scale neuroanatomy of the entire mouse brain

L. Silvestri,[1,*] A. Bria,[2,3] L. Sacconi,[1,4] G. Iannello,[2] and F. S. Pavone[1,4,5,6]

[1] *European Laboratory for Non-Linear Spectroscopy (LENS), University of Florence, Italy*
[2] *Integrated Research Centre, University Campus Bio-Medico of Rome, Italy*
[3] *Department of Automation, Electromagnetism, Information Engineering and Industrial Mathematics (DAEMI), University of Cassino, Italy*
[4] *National Institute of Optics, National Research Council, Italy*
[5] *Department of Physics, University of Florence, Italy*
[6] *International Center of Computational Neurophotonics (ICON), Italy*
[*] *silvestri@lens.unifi.it*

Abstract: Elucidating the neural pathways that underlie brain function is one of the greatest challenges in neuroscience. Light sheet based microscopy is a cutting edge method to map cerebral circuitry through optical sectioning of cleared mouse brains. However, the image contrast provided by this method is not sufficient to resolve and reconstruct the entire neuronal network. Here we combined the advantages of light sheet illumination and confocal slit detection to increase the image contrast in real time, with a frame rate of 10 Hz. In fact, in confocal light sheet microscopy (CLSM), the out-of-focus and scattered light is filtered out before detection, without multiple acquisitions or any post-processing of the acquired data. The background rejection capabilities of CLSM were validated in cleared mouse brains by comparison with a structured illumination approach. We show that CLSM allows reconstructing macroscopic brain volumes with sub-cellular resolution. We obtained a comprehensive map of Purkinje cells in the cerebellum of L7-GFP transgenic mice. Further, we were able to trace neuronal projections across brain of thy1-GFP-M transgenic mice. The whole-brain high-resolution fluorescence imaging assured by CLSM may represent a powerful tool to navigate the brain through neuronal pathways. Although this work is focused on brain imaging, the macro-scale high-resolution tomographies affordable with CLSM are ideally suited to explore, at micron-scale resolution, the anatomy of different specimens like murine organs, embryos or flies.

OCIS codes: (180.6900) Three-dimensional microscopy; (180.1790) Confocal microscopy.

References and links

1. C. Sotelo, "Viewing the brain through the master hand of Ramon y Cajal," Nat. Rev. Neurosci. **4**(1), 71–77 (2003).
2. J. Huisken and D. Y. Stainier, "Selective plane illumination microscopy techniques in developmental biology," Development **136**(12), 1963–1975 (2009).
3. P. J. Keller and H. U. Dodt, "Light sheet microscopy of living or cleared specimens," Curr. Opin. Neurobiol. **22**(1), 138–143 (2012).
4. P. J. Keller, F. Pampaloni, and E. H. Stelzer, "Life sciences require the third dimension," Curr. Opin. Cell Biol. **18**(1), 117–124 (2006).
5. J. Mertz, "Optical sectioning microscopy with planar or structured illumination," Nat. Methods **8**(10), 811–819 (2011).
6. J. A. Buytaert and J. J. Dirckx, "Design and quantitative resolution measurements of an optical virtual sectioning three-dimensional imaging technique for biomedical specimens, featuring two-micrometer slicing resolution," J. Biomed. Opt. **12**(1), 014039 (2007).

#168613 - $15.00 USD Received 15 May 2012; revised 9 Jul 2012; accepted 9 Jul 2012; published 23 Aug 2012

7. H. U. Dodt, U. Leischner, A. Schierloh, N. Jährling, C. P. Mauch, K. Deininger, J. M. Deussing, M. Eder, W. Zieglgänsberger, and K. Becker, “Ultramicroscopy: three-dimensional visualization of neuronal networks in the whole mouse brain,” Nat. Methods **4**(4), 331–336 (2007).
8. C. Dunsby, “Optically sectioned imaging by oblique plane microscopy,” Opt. Express **16**(25), 20306–20316 (2008).
9. E. Fuchs, J. Jaffe, R. Long, and F. Azam, “Thin laser light sheet microscope for microbial oceanography,” Opt. Express **10**(2), 145–154 (2002).
10. T. F. Holekamp, D. Turaga, and T. E. Holy, “Fast three-dimensional fluorescence imaging of activity in neural populations by objective-coupled planar illumination microscopy,” Neuron **57**(5), 661–672 (2008).
11. J. Huisken and D. Y. Stainier, “Even fluorescence excitation by multidirectional selective plane illumination microscopy (mSPIM),” Opt. Lett. **32**(17), 2608–2610 (2007).
12. J. Huisken, J. Swoger, F. Del Bene, J. Wittbrodt, and E. H. Stelzer, “Optical sectioning deep inside live embryos by selective plane illumination microscopy,” Science **305**(5686), 1007–1009 (2004).
13. P. J. Keller, A. D. Schmidt, J. Wittbrodt, and E. H. Stelzer, “Reconstruction of zebrafish early embryonic development by scanned light sheet microscopy,” Science **322**(5904), 1065–1069 (2008).
14. H. Siedentopf and R. Zsigmondy, “Uber Sichtbarmachung und Grössenbestimmung ultramikroskopischer Teilchen, mit besonderer Anwendung auf Goldrubingläser,” Annalen der Physik **10**, 1–39 (1903).
15. M. Tokunaga, N. Imamoto, and K. Sakata-Sogawa, “Highly inclined thin illumination enables clear single-molecule imaging in cells,” Nat. Methods **5**(2), 159–161 (2008).
16. P. J. Verveer, J. Swoger, F. Pampaloni, K. Greger, M. Marcello, and E. H. Stelzer, “High-resolution three-dimensional imaging of large specimens with light sheet-based microscopy,” Nat. Methods **4**(4), 311–313 (2007).
17. A. H. Voie, D. H. Burns, and F. A. Spelman, “Orthogonal-plane fluorescence optical sectioning: three-dimensional imaging of macroscopic biological specimens,” J. Microsc. **170**(3), 229–236 (1993).
18. S. Kalchmair, N. Jährling, K. Becker, and H. U. Dodt, “Image contrast enhancement in confocal ultramicroscopy,” Opt. Lett. **35**(1), 79–81 (2010).
19. P. J. Keller, A. D. Schmidt, A. Santella, K. Khairy, Z. Bao, J. Wittbrodt, and E. H. Stelzer, “Fast, high-contrast imaging of animal development with scanned light sheet-based structured-illumination microscopy,” Nat. Methods **7**(8), 637–642 (2010).
20. J. Mertz and J. Kim, “Scanning light-sheet microscopy in the whole mouse brain with HiLo background rejection,” J. Biomed. Opt. **15**(1), 016027 (2010).
21. F. O. Fahrbach and A. Rohrbach, “Propagation stability of self-reconstructing Bessel beams enables contrast-enhanced imaging in thick media,” Nat Commun **3**, 632 (2012).
22. M. Tomomura, D. S. Rice, J. I. Morgan, and M. Yuzaki, “Purification of Purkinje cells by fluorescence-activated cell sorting from transgenic mice that express green fluorescent protein,” Eur. J. Neurosci. **14**(1), 57–63 (2001).
23. G. Feng, R. H. Mellor, M. Bernstein, C. Keller-Peck, Q. T. Nguyen, M. Wallace, J. M. Nerbonne, J. W. Lichtman, and J. R. Sanes, “Imaging neuronal subsets in transgenic mice expressing multiple spectral variants of GFP,” Neuron **28**(1), 41–51 (2000).
24. J. A. Conchello and J. W. Lichtman, “Optical sectioning microscopy,” Nat. Methods **2**(12), 920–931 (2005).
25. W. Spalteholz, *Uber das Durchsichtigmachen von menschlichen und tierischen Präparaten und seine theoretischen Bedingungen, nebst Anhang: Uber Knochenfärbung.* (S. Hirzel, Leipzig, 1914).
26. M. J. Booth and T. Wilson, “Refractive-index-mismatch induced aberrations in single-photon and two-photon microscopy and the use of aberration correction,” J. Biomed. Opt. **6**(3), 266–272 (2001).
27. T. Wilson and A. R. Carlini, “Size of the detector in confocal imaging systems,” Opt. Lett. **12**(4), 227–229 (1987).
28. G. Cox and C. J. Sheppard, “Practical limits of resolution in confocal and non-linear microscopy,” Microsc. Res. Tech. **63**(1), 18–22 (2004).
29. J. Jankowski, A. Miething, K. Schilling, and S. L. Baader, “Physiological purkinje cell death is spatiotemporally organized in the developing mouse cerebellum,” Cerebellum **8**(3), 277–290 (2009).
30. J. Altman and S. A. Bayer, “Embryonic development of the rat cerebellum. III. Regional differences in the time of origin, migration, and settling of Purkinje cells,” J. Comp. Neurol. **231**(1), 42–65 (1985).
31. R. R. Buss, W. Sun, and R. W. Oppenheim, “Adaptive roles of programmed cell death during nervous system development,” Annu. Rev. Neurosci. **29**(1), 1–35 (2006).
32. M. Bauman and T. L. Kemper, “Histoanatomic observations of the brain in early infantile autism,” Neurology **35**(6), 866–874 (1985).
33. T. L. Kemper and M. Bauman, “Neuropathology of infantile autism,” J. Neuropathol. Exp. Neurol. **57**(7), 645–652 (1998).
34. E. R. Ritvo, B. J. Freeman, A. B. Scheibel, T. Duong, H. Robinson, D. Guthrie, and A. Ritvo, “Lower Purkinje cell counts in the cerebella of four autistic subjects: initial findings of the UCLA-NSAC Autopsy Research Report,” Am. J. Psychiatry **143**(7), 862–866 (1986).
35. M. Helmstaedter, K. L. Briggman, and W. Denk, “3D structural imaging of the brain with photons and electrons,” Curr. Opin. Neurobiol. **18**(6), 633–641 (2008).
36. J. W. Lichtman, J. Livet, and J. R. Sanes, “A technicolour approach to the connectome,” Nat. Rev. Neurosci. **9**(6), 417–422 (2008).

37. O. Sporns, G. Tononi, and R. Kötter, "The human connectome: A structural description of the human brain," PLOS Comput. Biol. **1**(4), e42 (2005).
38. K. L. Briggman, M. Helmstaedter, and W. Denk, "Wiring specificity in the direction-selectivity circuit of the retina," Nature **471**(7337), 183–188 (2011).
39. W. K. Jeong, J. Schneider, S. G. Turney, B. E. Faulkner-Jones, D. Meyer, R. Westermann, R. C. Reid, J. Lichtman, and H. Pfister, "Interactive histology of large-scale biomedical image stacks," IEEE Trans. Vis. Comput. Graph. **16**(6), 1386–1395 (2010).
40. S. Mori, K. Oishi, and A. V. Faria, "White matter atlases based on diffusion tensor imaging," Curr. Opin. Neurol. **22**(4), 362–369 (2009).
41. W. R. Zipfel, R. M. Williams, and W. W. Webb, "Nonlinear magic: multiphoton microscopy in the biosciences," Nat. Biotechnol. **21**(11), 1369–1377 (2003).
42. T. A. Planchon, L. Gao, D. E. Milkie, M. W. Davidson, J. A. Galbraith, C. G. Galbraith, and E. Betzig, "Rapid three-dimensional isotropic imaging of living cells using Bessel beam plane illumination," Nat. Methods **8**(5), 417–423 (2011).
43. H. Hama, H. Kurokawa, H. Kawano, R. Ando, T. Shimogori, H. Noda, K. Fukami, A. Sakaue-Sawano, and A. Miyawaki, "Scale: a chemical approach for fluorescence imaging and reconstruction of transparent mouse brain," Nat. Neurosci. **14**(11), 1481–1488 (2011).
44. K. Becker, N. Jährling, S. Saghafi, R. Weiler, and H. U. Dodt, "Chemical clearing and dehydration of GFP expressing mouse brains," PLoS ONE **7**(3), e33916 (2012).
45. A. Ertürk, C. P. Mauch, F. Hellal, F. Förstner, T. Keck, K. Becker, N. Jährling, H. Steffens, M. Richter, M. Hübener, E. Kramer, F. Kirchhoff, H. U. Dodt, and F. Bradke, "Three-dimensional imaging of the unsectioned adult spinal cord to assess axon regeneration and glial responses after injury," Nat. Med. **18**(1), 166–171 (2011).
46. U. Krzic, S. Gunther, T. E. Saunders, S. J. Streichan, and L. Hufnagel, "Multiview light-sheet microscope for rapid in toto imaging," Nat. Methods **9**(7), 730–733 (2012).
47. R. Tomer, K. Khairy, F. Amat, and P. J. Keller, "Quantitative high-speed imaging of entire developing embryos with simultaneous multiview light-sheet microscopy," Nat. Methods **9**(7), 755–763 (2012).
48. A. Li, H. Gong, B. Zhang, Q. Wang, C. Yan, J. Wu, Q. Liu, S. Zeng, and Q. Luo, "Micro-optical sectioning tomography to obtain a high-resolution atlas of the mouse brain," Science **330**(6009), 1404–1408 (2010).
49. D. Mayerich, L. Abbott, and B. McCormick, "Knife-edge scanning microscopy for imaging and reconstruction of three-dimensional anatomical structures of the mouse brain," J. Microsc. **231**(1), 134–143 (2008).
50. N. Jährling, K. Becker, C. Schönbauer, F. Schnorrer, and H. U. Dodt, "Three-dimensional reconstruction and segmentation of intact Drosophila by ultramicroscopy," Front Syst Neurosci **4**, 1 (2010).
51. A. B. Arrenberg, D. Y. Stainier, H. Baier, and J. Huisken, "Optogenetic control of cardiac function," Science **330**(6006), 971–974 (2010).
52. A. Bria, L. Silvestri, L. Sacconi, F. S. Pavone, and G. Iannello, "Stitching Terabyte-sized 3D images acquired in confocal ultramicroscopy," presented at the *IEEE International Symposium on Biomedical Imaging* (ISBI 2012), Barcelona, Spain, 2–5 May 2012.
53. P. J. Bex and W. Makous, "Spatial frequency, phase, and the contrast of natural images," J. Opt. Soc. Am. A **19**(6), 1096–1106 (2002).

---

1. Introduction

More than a century after the pioneering work of Ramon y Cajal, that gave the first insights into the peculiar structure of nervous tissue, we still lack a comprehensive map of neuronal projections throughout the whole brain [1]. This is mainly due to the unique anatomical organization of the brain, in which microscopic neuronal processes span for macroscopic distances. Mapping of neuronal projections would require large volumes (~1 cm^3 for mice brain) reconstruction with sub-micrometric resolution.

A promising tool to optically reconstruct neuronal connections through the whole brain with high resolution is light sheet based microscopy (LSM) [2–5]. In this technique the sample is illuminated with a thin sheet of light and the fluorescence emission is collected along an axis perpendicular to the plane of illumination [6–17]. This approach confines the excitation light to the focal plane allowing optical sectioning in wide-field detection architecture. Coupled to optical clearing procedures, based on refractive index matching, LSM has been recently applied to image fixed mouse brains [7]. Although this method allows sub-cellular high-contrast imaging in excised regions, sample-induced light scattering prevents high-resolution imaging in the whole brain. In fact, the residual sample-induced scattering that still affects a cleared brain expands the excitation light sheet (leading to out-of-focus contributions) and blurs the collected fluorescence images.

Several strategies have been proposed in LSM to recover the original contrast reduced by sample-induced light scattering. Structured illumination (SI) patterns [18, 19] or spatial frequency information of the acquired images [20] have been recently exploited to reject the out-of-focus background. These approaches provide a remarkable background rejection, but in general they require redundant images acquisition and, in some cases, definition of post-processing *ad hoc* parameters to synthesize the output images.

Recently, Fahrbach and Rohrbach [21] have developed an alternative method (CL-MISERB) to reject out of focus background in LSM based on confocal line detection. In this method the light sheet is obtained scanning a Bessel beam following the same principle of digital scanned light sheet microscopy (DSLM) [13]. During scanning a CCD camera is exposed and read out for every different position of the excitation beam, until the whole field of view is covered. A post-processing algorithm then extract from each acquired image the intensity profile of the line corresponding to the position of the scanning beam, acting as a confocal pinhole. The intensity profiles are finally combined in a 2D image in which the out-of-focus light has been filtered out.

Here we describe an optical method, confocal light sheet microscopy (CLSM), in which the out-of-focus background rejection based on confocal detection is achieved in real time. CLSM synergically combines the advantages of LSM, in terms of fast acquisition time and low photobleaching rate, with the spatial filtering capability of a confocal approach. The capability of CLSM in background rejection has been validated by comparison with SI-based LSM. The potential applicability of CLSM in brain imaging was probed by resolving the fine neuroanatomy of Purkinje cells in the whole cerebellum of L7-GFP transgenic mice [22]. The whole-brain high-resolution capability was demonstrated by imaging the entire network of labeled neurons in a thy1-GFP-M transgenic mouse [23]. We show that the resolution and contrast of CLSM allows resolving and following a single process inside an entire brain opening promising prospective in neuronal mapping.

Having to deal with macroscopic samples, CLSM had to face another challenge: managing and processing a large quantity of data. In fact, assuming that the volume is sampled using cubic voxels with 1 µm side, and represented using a 8-bit grayscale, a cube with a side of ≈1 cm (mouse brain) would require about one TeraByte of disk space. *Ad hoc* designed image processing tools allowing the reconstruction and the analysis of very large data sets have been developed for this purpose.

2. Results

2.1 Confocal light sheet microscopy (CLSM)

The key feature of CLSM is a spatial filter that selects only ballistic fluorescence photons emitted from the focal plane of detection optics, i.e. from fluorophores excited by ballistic illumination photons. To apply a spatial filter in light sheet based architecture we obtain the illumination plane by means of a scanning line as in DSLM [13]. We then coupled the excitation scanning system with a detection de-scanning which images the excitation scanning line as a static line in a secondary plane (Fig. 1(b) and Media 1). In this position a linear spatial filter (slit) is placed. After the slit, a third scanning system reconstructs the planar image on an EM-CCD camera sensor. Since the slit aperture is placed in an image plane of the system, no diffraction fringes are expected in the conjugate image plane where the camera sensor is placed. Whilst in point-scanning confocal microscopy fluorescence light passes through the same deflection system used for excitation [24], in CLSM the illumination and detection paths are separated, making synchronization between different scanning systems crucial. In our system, stable synchronization was assured by a data acquisition (DAQ) board with high timing resolution and accuracy.

#168613 - $15.00 USD Received 15 May 2012; revised 9 Jul 2012; accepted 9 Jul 2012; published 23 Aug 2012

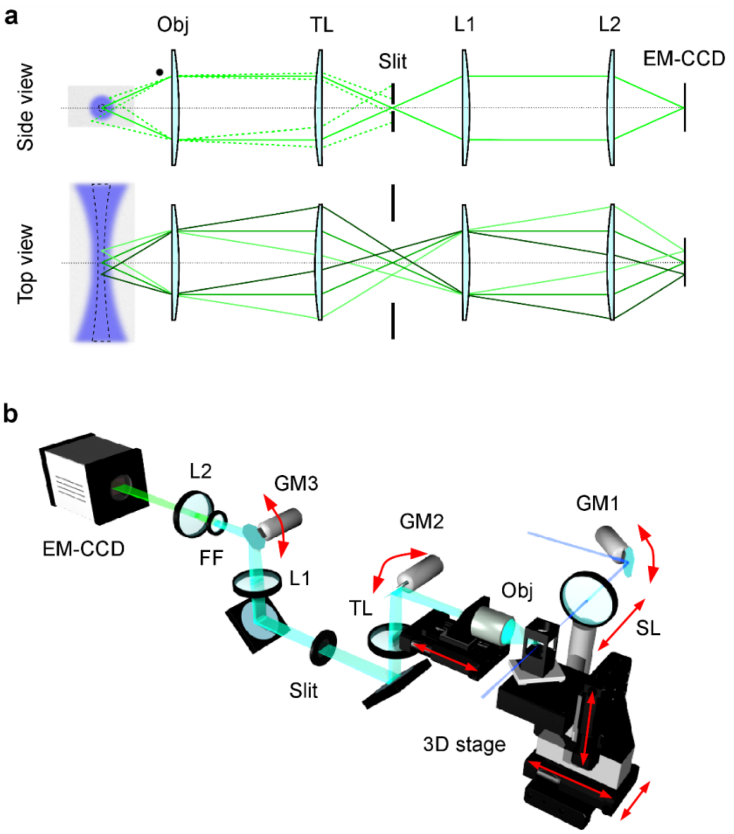

Fig. 1. Confocal light sheet microscopy (CLSM). (a) Side (upper panel) and top (lower panel) views of the spatial filter operation scheme. The diffraction limited excitation beam (black dashed line) is blurred (blue area) because of sample-induced scattering. The fluorescence light is then emitted both in-focus (green continuous lines) and out-of-focus (green dashed lines): only the in-focus ballistic photons are properly focused in the aperture of the spatial filter (Slit) by the first 4f optical system (objective, Obj and tube lens, TL). The second 4f system (L1, L2) images ballistic photons on the EM-CCD sensor. In the top view, rays originating from different positions are depicted with different hues of green. (b) CLSM optical scheme. The excitation laser beam is scanned by a first galvo mirror (GM1) and focused by a scanning lens (SL) on the specimen. The fluorescence emission orthogonally collected by Obj is de-scanned by a second galvo (GM2) pivoting the linear image onto the slit aperture. A third scanning mirror (GM3) recreates the wide field-like image on the EM-CCD sensor after filtering out of the excitation light by a fluorescence filter (FF). Precision micro-translators allow both 3D motion of the specimen chamber (3D stage) and the movement of excitation (SL) and detection (Obj) optics.

In LSM, deep imaging of macroscopic samples is allowed by a procedure to clear tissue based on the immersion of the brain in a medium (Benzyl Alcohol and Benzyl Benzoate 1:2, BABB) with the same refractive index as proteins [7, 25]. A custom-made chamber was designed to keep the sample immersed in clearing solution during imaging sessions. An air objective lens was used, providing sufficient working distance to image whole mouse brains without sample sectioning. Due to the interface between air and clearing solution, the actual focal length of both excitation and detection lenses depend on the position of the imaged plane inside the specimen chamber. Scanning lens (SL in Fig. 1(b)) and objective (Obj in Fig. 1(b)) were motorized, and their positions were adjusted in real time to compensate the shift of focus.

Received 15 May 2012; revised 9 Jul 2012; accepted 9 Jul 2012; published 23 Aug 2012

The 20 × magnification of our long working distance microscope objective allows to expose the EM-CCD sensor with a field of view of ≈400 × 400 μm^2. Imaging of macroscopic specimens was achieved through a set of high precision translation stages that move the sample in order to acquire multiple parallel adjacent stacks of images covering the whole volume (Fig. 1(b)). We found that, due to slight imperfections in the right-angle arrangement of the motors and to deformation of the agarose gel in which the sample is embedded (see Methods), adjacent stacks are slightly misaligned. Typical misalignment between adjacent stacks ranges from 1 to 5 μm for stack lengths of the order of 1 cm. For this reason, an overlapping region of 50 μm has been introduced between adjacent tiles in order to automatically combine the stacks by means of a 3D-stitching tool designed to process large amount of data (~1 TeraByte). The processing pipeline of the 3D-stitching tool starts with pairwise tile displacements computation, followed by globally optimal placement of tiles, and restoring/combination of tiles into a multi-resolution representation suited for visualization and further processing (see Methods). The alignment accuracy of the 3D-stitching tool depends on the signal to background ratio and on the characteristic texture of the stacks to be aligned. We found that in sub volumes filled with fluorescent neuronal structures the alignment accuracy was below the optical resolution of the system.

2.2 Spatial resolution and background rejection

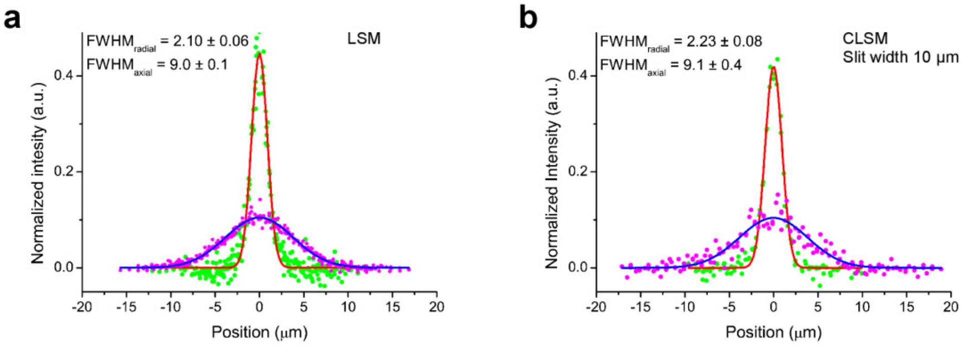

Fig. 2. Measurement of radial and axial CLSM point spread functions. Axial (purple circles) and radial (green circles) point spread functions (PSFs) measured in conventional (a) and in confocal modality (b). The best Gaussian fits for axial and radial PSFs are shown by the blue and red lines, respectively. Experimental data have been normalized in area.

The performance of our technique in terms of spatial resolution has been tested measuring the point spread function (PSF) of the optical system using sub-diffraction fluorescent beads (see Methods). We found that, in absence of the spatial filter, the full width at half maximum (FWHM) of the radial and axial PSF is (2.10 ± 0.06) μm and (9.0 ± 0.1) μm respectively (see Fig. 2(a)). Taking into account the numerical aperture (NA) of the objective (0.35), the NA of the scanning lens (0.0246), the refractive index of BABB (1.559) and the Gaussian nature of the excitation beam, we calculated the FWHM of the detection Airy disc (≈0.8 μm) and the thickness of the light sheet (≈7.4 μm). The illumination NA was chosen to obtain a confocal parameter ≈800 μm, the double of the field of view. While this choice guarantees a uniform illumination through the whole field of view, on the other hand such a large excitation beam reduces the axial resolution and the illumination efficiency of the system. In fact, we calculated that only ≈15% of the excitation Gaussian beam lies in the volume potentially imaged throughout the spatial filter. The non-negligible difference between calculated and measured values of PSF FWHM, predominantly on the radial component, is mainly attributable to spherical aberration [26]. In fact, the long working distance objective lens employed to image macroscopic samples is not corrected for the presence of ~10 mm of clearing solution in which the brain is immersed.

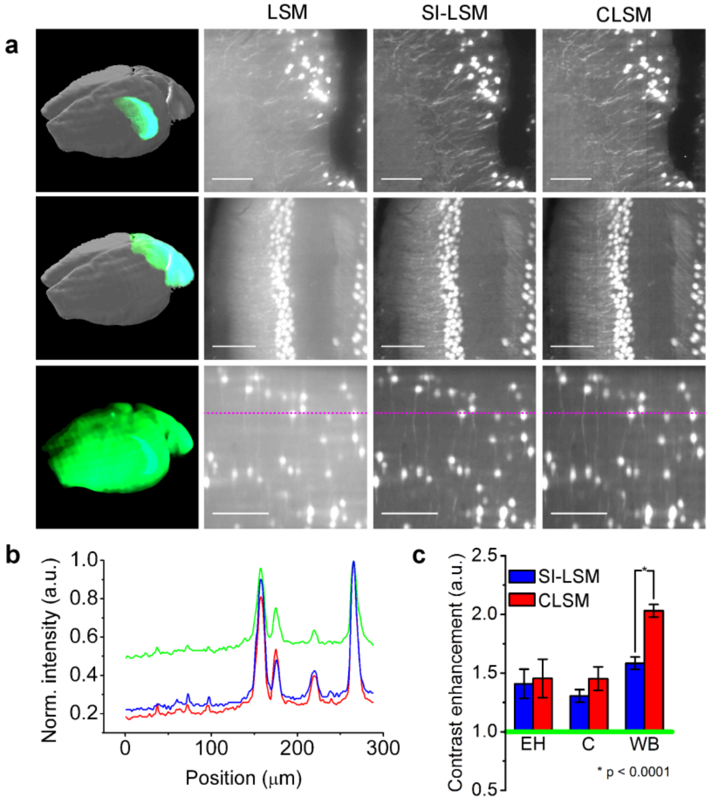

Fig. 3. Background rejection. (a) Comparison between LSM, SI-LSM and CLSM performed in: excised hippocampus (EH) of a thy1-GFP-M mouse, cerebellum (C) of a L7-GFP mouse and whole brain (WB) of a thy1-GFP-M mouse; post natal day (PND) 15 for all samples. Images are maximum intensity projections of 40 sections (z-step 1 μm). The lookup table saturates 4% of pixels for better visibility and comparison. Scale bars, 100 μm. (b) Intensity profiles (green: LSM; blue: SI-LSM; red: CLSM) along the dotted purple lines highlighted in panel (a). The profiles are normalized with respect to their maximum intensity value. (c) Contrast enhancement of SI-LSM (in blue) and CLSM (in red) with respect to LSM, calculated from data acquired in EH, C, WB. Each bar represents the mean and standard error of the mean. The green line refers to no contrast enhancement.

We found that, in the presence of the spatial filter, the radial and axial PSFs are (2.23 ± 0.08) μm and (9.1 ± 0.4) μm respectively (see Fig. 2(b)). These values are identical to those found without the slit, pointing out that the spatial filter in CLSM does not induce any significant spatial resolution enhancement. This result well correlates with the choice of a slit width comparable to the optical system PSF. In fact, like in confocal microscopy, in this configuration (i.e. when the spatial filter is comparable with the PSF) the resolution enhancement is negligible [27, 28].

Although the CLSM spatial filter does not introduce any resolution enhancement it is central in rejecting the out-of-focus background. This capability was tested comparing CLSM with conventional and SI-based LSM. We used the SI implementation described by Kalchmair *et al.* [18], since it has been applied to enhance image contrast in cleared mouse brains with similar magnification and resolution. The comparison was performed on specimens of different sizes: excised hippocampus, excised cerebellum and whole brain (Figs. 3 (a),3(b).

CLSM showed a remarkable background rejection in all the analyzed specimens. Figure 3(c) quantitatively compares the contrast enhancement of CLSM and SI-LSM with respect to conventional LSM (see Methods). We found that, in excised specimens, the contrast enhancement provided by CLSM is comparable to that of the SI-LSM implementation used and, in whole brains, it is even higher (t-test based). The use of an objective lens with higher numerical aperture better highlights the CLSM background rejection capabilities (Fig. 4).

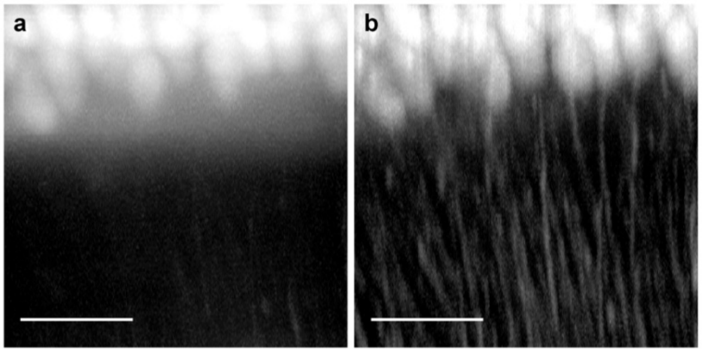

Fig. 4. Background rejection using higher NA optics. Purkinje cells in the cerebellum of a PND 15 L7-GFP mouse, imaged with LSM (a) and CLSM (b) using an objective with higher numerical aperture (Nikon 50 × , NA = 0.45). Slit width was 15 µm, corresponding to 0.6 µm in object space. Images are maximum intensity projections of 160 sections (z-step 1 µm). For better visibility and comparison a nonlinear gamma transformation ($\gamma = 0.35$) was applied to the images, and the lookup table was linearly modified to eliminate 4% outliers. Scale bars, 100 µm

It is worth noting that CLSM is actually 1D confocal: while the majority of scattered photons are blocked, those photons scattered along the slit can still be collected by the EM-CCD, adding background noise. The fraction of scattered photons entering the slit depends on the spatial spreading of the scattered halo. In general, the percentage of photons entering the spatial filter increases linearly with the extent of the scattered halo. Indeed, we observed that deeper inside the tissue the intensity of the images drops, while the background light slightly increases. On the other hand, we did not found any significant enlargement of the point spread function of the system but rather a contrast decrease. Despite these limiting factors, the system is still capable of imaging neuronal processes in core brain regions.

2.3 Optical tomography of the entire brain

The macro-scale high-resolution imaging capability of our technique was first tested on the whole cerebellum of a L7-GFP mouse, transgenic model in which all Purkinje cells (PC) are EGFP (enhanced green fluorescent protein) labeled (Fig. 5). The 3D reconstruction of all PCs (see Media 2) was performed imaging an excised cerebellum (total volume ≈73 mm^3) with a voxel dimension of 0.8 × 0.8 × 1 µm^3. The total volume was acquired in ≈24 h (≈20 min/mm^3) setting an EM-CCD exposure time of 100 ms per image section. Data were then processed in ≈14 h (≈11 min/mm^3).

Received 15 May 2012; revised 9 Jul 2012; accepted 9 Jul 2012; published 23 Aug 2012

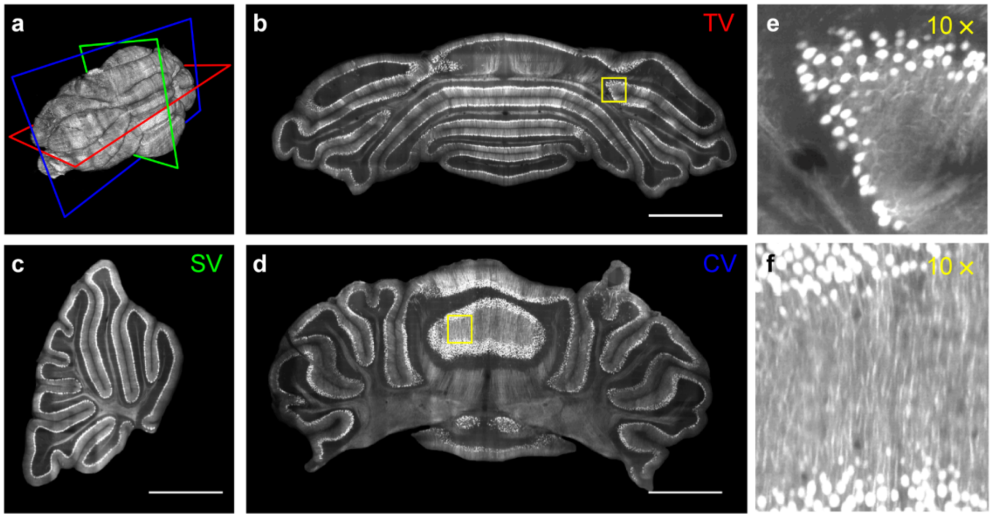

Fig. 5. Purkinje cells micron-scale neuroanatomy in the whole cerebellum. (a) 3D volume rendering of a PND-10 L7-GFP mouse cerebellum. The superimposed planes refer to transverse (red), sagittal (green) and coronal (blue) digital sections shown in panel (b), (c) and (d) respectively. (b-d) Maximum intensity projections of 40 µm thick slabs. Scale bars, 1 mm. (e, f) 10 × magnification of the regions highlighted by the yellow boxes in panels (b) and (d). The lookup table saturates 2% of pixels for better visibility.

Digital stereotaxic sections extracted from the 3D reconstruction (Figs. 5(b)-5(d)) revealed the well-known spatial organization of PCs within the cerebellum. As shown in Figs. 5(e) and 5(f), the contrast and resolution of CLSM allow resolving individual PC bodies and dendritic arbors. This result demonstrates the potential of CLSM in performing high-throughput screening of neuronal spatial organization, opening promising prospective in development studies [29–31] and neurodevelopmental disorders [32–34] investigations.

To investigate if data obtained with CLSM allows neuronal tracing we used transgenic mice characterized by intense and sparse labeling of a variety of neuronal subsets distributed in the whole brain (thy1-GFP-M). The optical tomography of a whole thy1-GFP-M mouse brain (total volume ≈223 mm^3) was acquired using the same voxel dimension and exposure time as before (see Media 3). From the three-dimensional reconstruction of the whole brain (Fig. 6(a)), we virtually dissected volumes from the hippocampus (Fig. 6(b)) and the superior colliculus (Fig. 6(c)). In both cases isolated neuronal processes can be clearly distinguished demonstrating the possibility of studying long-range projections tracing several neurites over a mm-sized volume (Fig. 6(d)) in a core region of the brain. By reverse, measurements performed using conventional LSM produced images with signal to background ratios insufficient to distinguish single processes in core brain regions (see also Fig. 3).

#168613 - $15.00 USD Received 15 May 2012; revised 9 Jul 2012; accepted 9 Jul 2012; published 23 Aug 2012

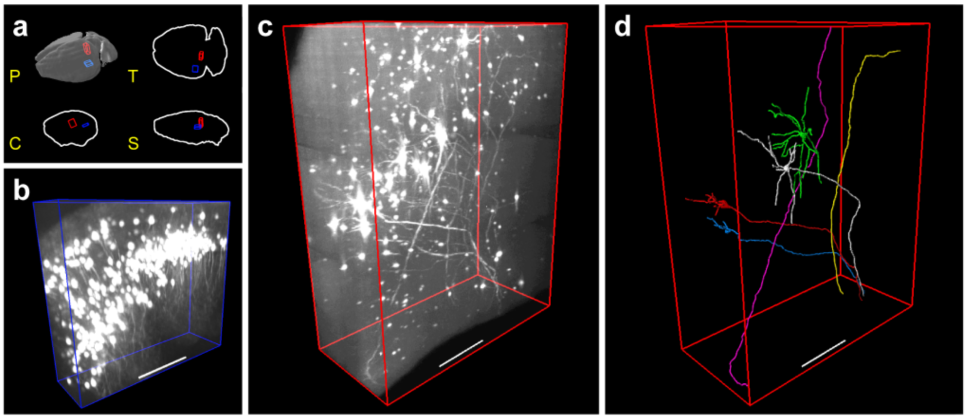

Fig. 6. Micron-scale neuroanatomy of a whole thy1-GFP-M brain. (a) Isosurface perspective (P) and transverse (T), coronal (C) and sagittal (S) contours of an entire PND-15 mouse brain. The volumes highlighted by the blue and red boxes are magnified in panel (b) and (c) respectively. (b) Volume rendering of a portion of hippocampus. (c) Volume rendering of a portion of superior colliculus. (d) Soma segmentation and process tracing of selected fluorescent neurons present in the red box (c). For clarity, each neuron was drawn with a different color. Scale bars, 200 μm.

3. Discussion

The cognitive and behavioral functions of the nervous system depend on the transmission of electrical signals within complex neural circuits. Although our understanding of the mechanisms underlying neuronal synapses has advanced in recent years, the knowledge of fine brain neuroanatomy lags a long way behind. The visualization of entire neuronal networks with sub-cellular resolution has been impossible up to now [35–37]. In fact, each method potentially beneficial to brain connectomics presents critical drawbacks that limit the real applicability (Table 1). For example, although the nm spatial resolution of electron microscopy (EM) makes it invaluable in the reconstruction of fine circuitry [38], the acquisition rate is too low to map large areas. Furthermore, the amount of data contained in a whole brain reconstruction with nm resolution will exceed the tens of PetaBytes, requiring outstanding efforts in information and communication technology [39]. On the other hand, MRI-based techniques like diffusion tensor imaging (DTI) allow fast reconstruction of large volumes *in vivo*, but at very poor resolution, much larger than the typical size of neuronal processes [40]. Furthermore, no specific labeling is applicable to DTI, limiting the classification of the observed fiber bundles.

An integrated approach may be proficient to face the challenge of neuronal mapping. In practice, this integration is quite difficult, mainly because of the non-overlapping operative range (in terms of spatial resolution, acquisition time, field of view, sample preparation, etc.) in which each technique operates. Optical methods can bridge the gap between high resolution in small volumes and low resolution in the whole brain. For example, the μm scale resolution of optical point-scanning techniques, like confocal [24] or multi-photon microscopy [41], is well suitable to correlate the nm with mm resolution ranges. However, the high numerical aperture objectives needed for these techniques makes mechanical slicing mandatory in large specimens, with consequent problems of layer misalignment and surface matching. Furthermore, the long acquisition time and the high photobleaching rate are inappropriate for whole brain imaging (Table 1).

Received 15 May 2012; revised 9 Jul 2012; accepted 9 Jul 2012; published 23 Aug 2012

Table 1. Comparison of Different Techniques for the Study of Neuronal Anatomy

Technique	Resolution	Acquisition speed ($\mu m^3/s$)	Total time to get useful data ($1\ cm^3$)*	Cell-specific
Electron microscopy	~$15 \times 15x50\ nm^3$	< 10	> 10^3 years	Yes
Point-scanning confocal microscopy	~$0.25x0.25x0.5\ \mu m^3$	~10^4	~3 years	Yes
Two-photon microscopy	~$0.5x0.5x1\ \mu m^3$	~10^4	~3 years	Yes
MOST/KESM	~$0.5x0.5x1\ \mu m^3$	~10^6	> 6 months	No
CLSM	~$2x2x9\ \mu m^3$	~10^6	< 1 month	Yes
High-field DTI	> $150x150x300\ \mu m^3$	~10^9	< 2 hours	No

* time for the full experimental pipeline including sample preparation, data acquisition and post-processing.

CLSM may overcome these optical limitations allowing imaging of a whole murine brain with µm scale resolution in less than one week without mechanical slicing. The data from EM, CLSM and DTI can be potentially integrated in a multi-scale/multi-resolution model carrying different kinds of information: local circuitry, long-range projections, *in vivo* time-lapse imaging.

Although CLSM allows sub-cellular imaging in the whole brain, the actual resolution is quite far from the diffraction limit. The interface between air and clearing solution induces spherical aberrations that reduce the quality of the collected images. Aberrations mainly affect detection, where an objective with moderate NA is used, while their effect in excitation is almost negligible, because of the low illumination NA. Corrected objective lenses or adaptive optical elements can be used to edit the optical wavefront and restore the diffraction limited resolution. Even in an aberration-free CLSM, the resolution remains highly anisotropic due to the difference in numerical aperture between illumination and detection optics. The resolution anisotropy can be compensated using several approaches based on Bessel beams [42] and/or multi-view tomography [16]. The Bessel beams approach would also improve illumination efficiency of the system.

Besides the decrease in resolution, another undesirable effect of spherical aberration is the drop of peak intensity of the PSF, since the light is spread on a wider area. In the observed samples, fluorescence is further reduced by dehydration in ethanol and clearing in BABB, which is known to quench emission from fluorescent proteins [43]. Here, this loss of signal has been compensated by setting a laser power close to the saturation value, a camera exposure time ≈100 ms, and using a detector with high signal to noise ratio in low photon flux regime (EM-CCD). Combining *ad hoc* aberration correction with novel clearing strategies that better preserve EGFP fluorescence [43–45], the CLSM optical scheme could be remarkably simplified by using a linear CCD sensor behind the slit.

A further simplification of the optical scheme can be accomplished, even in low photon flux regime, using new generation sCMOS sensors. In this case, the confocal detection could be achieved without the use of any descanning system in the detection path exploiting the rolling shutter modality present in these sensors. Considering the transmittance and the reflectivity of the optical elements present in the detection path, such a simplification would further reduce fluorescence losses of ≈15%.

In optical tomographies of the entire brain we do not observe significant resolution differences across the sample. However, especially in poorly cleared brains, we found contrast and brightness differences. Image contrast is better in the part of the brain closer to both excitation lens and detection objective, i.e. where both excitation and fluorescence light travel less inside the sample. On the other hand, image quality is worse in the opposite part of

Received 15 May 2012; revised 9 Jul 2012; accepted 9 Jul 2012; published 23 Aug 2012

the brain. Several workarounds to recover uniform image quality throughout the brain can be used, for example multi-direction tomography [16], as well as multi-direction excitation and detection [46, 47].

Due to the sample dimension we were forced to choose an air objective lens with a super long working distance. As described above, this aspect introduces a variable focal shift. In principle it would be possible to immerse the air objective lens in the BABB solution. In this case the defocusing will be fixed once, and there would be no further need for objective motorization. However, this will complicate the design of the specimen chamber/holder, to allow 3D relative motion of the sample with respect to the optics and will increase the amount of the spherical aberration. Custom-made super long working distance objectives designed for BABB would represent a big step ahead to overcome the current limitation of the apparatus.

Application of confocal line detection to LSM has been recently proposed by Fahrbach and Rohrbach [21] to suppress the external ring system present in Bessel beam illumination, which give rise to out-of-focus contributions. Although this confocal approach allows a significant enhancement of image contrast, the camera needs to be exposed and readout at each beam position to produce a single final image of the whole field of view, and background rejection is achieved by post-processing the acquired data. In CLSM, instead, out-of-focus light is filtered out in real time by a physical slit. The real time imaging assured by CLSM and the light sheet stability provided by Bessel beam illumination could be synergically combined enhancing imaging performances in scattering specimens.

Recently, a different technique addressing the neuroanatomy issue has been proposed: micro-optical sectioning tomography (MOST) [48]. This is an implementation of an approach known as knife-edge scanning microscopy (KESM) [49], in which the sample is embedded in a hard resin and imaged during slicing. These techniques allow reconstruction of whole mouse brains with optical resolution and in reasonable times (Table 1), but with two drawbacks: time-consuming sample preparation procedure and, most importantly, unspecific random labeling of neurons, based on the Golgi staining method. On the other hand the specificity of fluorescence labeling, on which CLSM relies, allows anatomical investigations of specific neuronal subsystems. For example, axonal projections of localized nuclei (like serotonergic or cholinergic systems), cortico-thalamic circuits, interhemispheric connections, etc. can be reconstructed using appropriate transgenic mouse models, retrograde labeling or viral strategies.

The usefulness of CLSM may not be limited to whole brain neuroanatomy but, as shown by standard light sheet based microscopy, can span different area of research. Anatomical studies of small organisms [7, 50] as well as of macroscopic organs [17], could be performed at micron-scale by means of CLSM. Live imaging of embryo development [12, 13] or of heart function [51] could take advantage of the high-contrast guaranteed by our technique. Finally, the real-time contrast enhancement achieved in CLSM may be useful in sub-cellular [42] and even single-molecule studies [15], opening the way to a wide spectrum of applications.

4. Methods

4.1 Confocal light sheet microscopy (CLSM)

The excitation light is provided by 50 mW CW externally doubled diode laser (Excelsior 488, Spectra Physics, CA), $\lambda = 488$ nm. The laser beam is expanded and collimated by a telescope and intensity modulated by an acousto-optic tunable filter (AOTF, AOTFnC-400.650-TN, AA Opto-Electronic, France). After a second beam expansion telescope, the beam passes through a $\lambda/2$ achromatic waveplate that maximize the fluorescence emission towards the detection axis. The laser beam is then scanned by a galvo mirror (VM2500 + , Cambridge Technology, MA) placed at 45° (see Fig. 1(b)) and focused by a scanning lens (focal length 50 mm) into a custom-made specimen chamber. In this configuration, a scanning angle of ± 4 mrad is used to cover a field of view of 400 µm. Within this operating range we calculated that the distortion of the light sheet is one order of magnitude smaller than its thickness. The fluorescence emission is collected by a long-working distance (24 mm) microscope objective (Plan SLWD 20 × , NA = 0.35, Nikon, Japan). When imaging smaller areas also another long-working distance (17 mm) microscope objective (Plan SLWD 50 × , NA = 0.45, Nikon, Japan) was used; this lens is however not suited for whole brain tomographies because the higher magnification would increase imaging time. The light emerging from the objective's back aperture is de-scanned by a second galvo mirror (VM2500 + , Cambridge Technology, MA), and imaged by a tube lens (TL) as a motionless line (see Fig. 1(b) and Video S1). We use a TL with a focal length of 100 mm, providing a magnification of 10 × in the image plane, where a mounted air slit (p/n 35290NR, JML Optical, NY) is placed. In CLSM modality, a slit width of 10 µm (corresponding to 1 µm in the object plane) is used. In conventional or structured illumination (SI) modalities the slit was absent. A second 4f imaging system (2 × magnification) reconstructs the image on the sensor (512 × 512 pixels, pixel size 16 × 16 μm^2) of an electron multiplying charge coupled device (EM-CCD, Cascade II: 512, Photometrics, AZ) restoring the design magnification of the objective lens (20 ×). Between the two lenses of the second 4f imaging system, a third galvo mirror (VM2500 + , Cambridge Technology, MA) deflects the light to reproduce the angular spreading of the beams emerging from the objective. An EGFP band pass (507-527 nm) fluorescence filter (BrightLine FF01-517/20-25, Semrock, NY) is used (see Fig. 1(b)). Due to the autofluorescence contributions which affect aldehyde-fixed tissues, the filter bandwidth was properly chosen to maximize the signal to background ratio. All lenses, with the exception of the first telescope in the excitation path, are achromatic doublets (CVI Melles Griot, NM).

To image different planes inside the sample, the specimen chamber is equipped with a motorized system made of three micro-positioning stages (M-122.2DD, Physik Instrumente, Germany) mounted along three perpendicular axes (see Fig. 1(b)). The sample is fixed inside the chamber on the top of a metallic pedestal disc watertight coupled to a rotation stage (M-116.DG, Physik Instrumente, Germany). The rotation stage usefully increases the flexibility of the system in terms of sample manipulation and will be a central element in future development of multi-view tomographic strategies (see Discussion).

The employment of a high refractive index clearing solution introduces a change in the effective focal length of excitation and detection optics. We call f the focal length in air, f' the effective focal length, d the distance between the interface and the nominal focus, and d' the distance between the interface and the effective focus. In paraxial approximation, it is straightforward to find:

$$f' - f = d' - d \approx d'\left(1 - 1/n\right) \approx 0.36\, d' \qquad (1)$$

The defocusing introduced by the interface is thus linearly dependent on the distance between the imaged plane and the interface (d'). This equation has been experimentally verified moving the sample (excised hippocampus) in z direction and refocusing the image by objective translation. To compensate variable focal shift due to the interface between air and clearing solution, the scanning lens and the microscope objective are mounted on motorized stages (M-111.1DG and M-122.2DD respectively, Physik Instrumente, Germany).

In CLSM, illumination and detection optical paths are independent, as well as the scanning and descanning systems. For this reason, the timing of the apparatus is crucial to achieve proper functioning (Media 1). To this end, the synchronization of the three galvo mirrors, the acousto-optic tunable filter (AOTF) and the electron multiplying charge-coupled device (EM-CCD) is mandatory. We implement a master and slave hierarchy, setting the EM-CCD in free-run mode and using a timing signal from the EM-CCD (master) to synchronize operation of the other items (slaves). In details, the timing provided by the master (TTL signal) is connected to a multi-function data acquisition device (NI PCI-6259, National Instruments, TX) and used to trigger the generation of triangular waves sent to the galvo

Received 15 May 2012; revised 9 Jul 2012; accepted 9 Jul 2012; published 23 Aug 2012

mirrors drivers. When the system operates in structured illumination modality (see below), the TTL triggers also the generation of a squared-wave signal sent to the AOTF to switch light on and off during scanning.

4.2 Structured Illumination (SI) modality

In SI modality we use the approach described by Kalchmair et al. [18]. Briefly, the illumination pattern is formed by 10 µm wide bright stripes placed every 100 µm (duty cycle 1:10). Twenty images are then acquired shifting the pattern by 5 µm for each step. The maximum and the minimum intensity values for each pixel are extracted from the images relative to different illumination patterns. Pixel value of the output images are obtained according to:

$$I(x,y) = \max_{i=1,\dots,20} I_i(x,y) - \gamma \min_{i=1,\dots,20} I_i(x,y) \tag{2}$$

where γ is a scaling factor (set = 0.5) and $I_i(x,y)$ is the intensity value of the i-th image at (x,y) position. The illumination pattern is realized switching on and off the beam during scanning using the AOTF.

4.3 Experimental CLSM resolution

To measure experimental PSF we prepared a phantom sample embedding silica core-shell fluorescent microbeads (45 nm of diameter; C-dot, Hybrid Silica Technologies, MA) in a 6% w/w agarose gel prepared in pure water. Beads concentration was about $10^3 \div 10^4$ beads/mm^3. The fluorescent dye inside the microbeads is fluorescein isothiocyanate, which shows absorption and emission spectra similar to EGFP. Phantom gels were dehydrated in ethanol/water 1:1 for 4 hours and then in pure ethanol overnight. After dehydration, phantoms were incubated in clearing solution for 1 day, and then imaged both in conventional and confocal modalities. We acquired several stacks of images (1 µm z-step) for each imaging modality; from these images radial and axial profiles of 10 beads were extracted. Beads profile were fitted with a Gaussian curve, and afterwards normalized (in area) and centered using the results of the fit. Normalized and centered profiles which were relative to the same experimental condition were then merged in a single data file (Fig. 2). These points were then fitted with a Gaussian curve (Fig. 2) using Origin Pro 8.1 (OriginLab, MA).

4.4 Sample preparation

Young mice (from PND-10 to PND-15) were deeply anesthetized by hypothermia and intraperitoneal injection of tribromoethanol (220 mg/kg), and transcardially perfused with 0.1 M PBS (pH 7.4) followed by 4% paraformaldehyde in 0.1 M PBS for fixation. Afterwards, the brain was removed from the skull, placed in fixative overnight at 4 °C and stored in PBS at 4 °C. We dissected out the desired brain region (if needed) and embedded the sample in a 0.5% (w/w) low melting point agarose gel prepared in 10 mM sodium borate buffer (pH 8). The embedded tissue was dehydrated in a graded ethanol series: for excised hippocampi and cerebella 30%, 50%, 80%, 96% 2 h each, then 100% overnight, while for whole brains 30%, 50%, 80%, 96%, 100% 12h each, the last step twice. The ethanol was diluted in sodium borate buffer to avoid considerable pH variations that would possibly decrease EGFP fluorescence. For whole brains, following Dodt et al. [7], we performed an extra dehydration step in 100% hexane for 1h after the graded ethanol series. After dehydration, we put the specimens in freshly prepared clearing solution composed of 1:2 Benzyl Alcohol and Benzyl Benzoate. The incubation time before imaging was ~36 h for excised hippocampi and cerebella, and ~3 d for whole brains. All dehydration/clearing steps were performed at room temperature (18-22 °C). All animal experiments performed comply with the guide for the care and use of laboratory animals.

#168613 - $15.00 USD Received 15 May 2012; revised 9 Jul 2012; accepted 9 Jul 2012; published 23 Aug 2012

4.5 From raw data to 3D image

Due to the limited field of view of our EM-CCD sensor, optical tomographies of macroscopic specimens require many parallel stacks of images to cover all the volume. To minimize data acquisition from empty areas, pre-tomography sampling is performed to roughly map sample shape and position.

The raw images are saved in real time in a dedicated workstation for further processing and analysis. To manage the TB of data stemming from whole brain tomography, the workstation was equipped with 96 GB of RAM, 9 TB of disk space, 2 quad-core CPUs at 2.26 GHz and a graphics card with 1 GB of dedicated memory. The acquired stacks are organized in a file hierarchy composed of two levels of directories, identifying the vertical (y) and horizontal (x) positions of a stack, respectively. Each second-level directory contained the stack as a sequence of consecutive image slices labeled with their position along the detection axis (z). A stitching tool capable to deal with teravoxel-sized 3D images has been developed. The stitching process, which is completely automatized, is schematically depicted in Fig. 7. It starts with a displacement computation for each pair of adjacent stacks according to a multi-MIP-NCC approach described as follows. The two stacks are split along the z axis into substacks of 100 slices. For each couple of homologous substacks, two overlapping regions are extracted using tile positions provided by the instrument. Since the size of the these regions is ~10 times larger than typical image drifts caused by the apparatus, the nominal alignment used at this stage assures that the overlapping regions actually overlap for most of their volume. These regions are aligned performing a 2D normalized cross-correlation (NCC) over maximum intensity projections (MIP) along the three axes. This provides two displacements for each direction and two associated parameters (in the following, *error measures*) estimating how reliable these displacements are. All this information is used to determine both the most reliable displacement between the two stacks and its associated error measure. Since the pairwise tile displacements obtained are not independent, a globally optimal placement of tiles is computed by finding the minimum spanning tree of the graph of stacks using the above mentioned error measures as displacement weights. Then, all tiles are combined into a single 3D image where the overlapping regions are substituted by a blended version of them to render the final image more homogeneous in the passage between adjacent stacks. Except this small correction no other intensity adjustment is applied to the final images. Two sinusoidal functions phase-shifted by π are used for weighting corresponding pixels. Finally, the resulting image is saved into a multiresolution representation possibly organized in a non-overlapping multi-stack format to improve memory efficiency of further processing. Further details about the stitching tool can be found in [52].

#168613 - $15.00 USD Received 15 May 2012; revised 9 Jul 2012; accepted 9 Jul 2012; published 23 Aug 2012

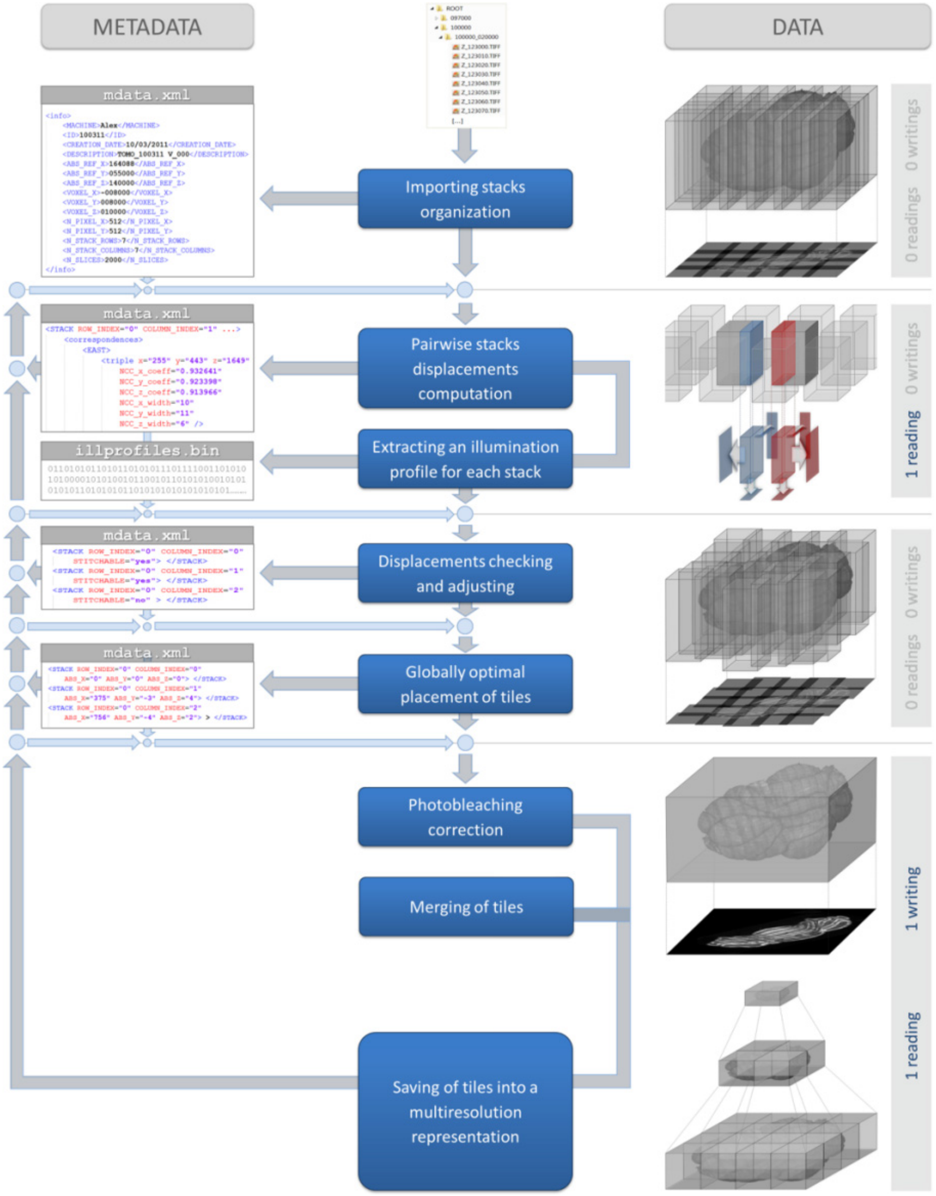

```
<info>
    <MACHINE>Alex</MACHINE>
    <ID>100311</ID>
    <CREATION_DATE>10/03/2011</CREATION_DATE>
    <DESCRIPTION>TOMO_100311 V_000</DESCRIPTION>
    <ABS_REF_X>164088</ABS_REF_X>
    <ABS_REF_Y>055000</ABS_REF_Y>
    <ABS_REF_Z>140000</ABS_REF_Z>
    <VOXEL_X>-008000</VOXEL_X>
    <VOXEL_Y>008000</VOXEL_Y>
    <VOXEL_Z>010000</VOXEL_Z>
    <N_PIXEL_X>512</N_PIXEL_X>
    <N_PIXEL_Y>512</N_PIXEL_Y>
    <N_STACK_ROWS>7</N_STACK_ROWS>
    <N_STACK_COLUMNS>7</N_STACK_COLUMNS>
    <N_SLICES>2000</N_SLICES>
</info>
```

```
<STACK ROW_INDEX="0" COLUMN_INDEX="1" ...>
    <correspondences>
        <EAST>
            <triple x="255" y="443" z="1649"
                NCC_x_coeff="0.932641"
                NCC_y_coeff="0.923398"
                NCC_z_coeff="0.913966"
                NCC_x_width="10"
                NCC_y_width="11"
                NCC_z_width="6" />
```

```
0110101011010110101011101111001101010
1010000101010010110010110101010010101
0101011010101011010101010101010101......
```

```
<STACK ROW_INDEX="0" COLUMN_INDEX="0"
    STITCHABLE="yes"> </STACK>
<STACK ROW_INDEX="0" COLUMN_INDEX="1"
    STITCHABLE="yes"> </STACK>
<STACK ROW_INDEX="0" COLUMN_INDEX="2"
    STITCHABLE="no" > </STACK>
```

```
<STACK ROW_INDEX="0" COLUMN_INDEX="0"
   ABS_X="0" ABS_Y="0" ABS_Z="0"> </STACK>
<STACK ROW_INDEX="0" COLUMN_INDEX="1"
   ABS_X="375" ABS_Y="-3" ABS_Z="4"> </STACK>
<STACK ROW_INDEX="0" COLUMN_INDEX="2"
   ABS_X="756" ABS_Y="-4" ABS_Z="2"> > </STACK>
```

Fig. 7. Stitching processing pipeline. All the processing steps and their action on both data and metadata are illustrated. On the right, for each step, it is indicated the number of reading and writing operations. Steps that are performed at the same time are connected with arrowless lines.

4.6 Image analysis

3D images were analyzed using Amira 5 (Visage Imaging, Australia) equipped with the Very Large Data Pack option. Simple image analysis was also performed through an open source imaging processing software (ImageJ). For better visualization, all the images were subjected to a linear transformation decreasing the maximum level of the lookup table (see Fig. Legends). Contrast enhancement reported in Fig. 3(c) was calculated according to Keller et al. [19]: each image was first normalized with total intensity, then the standard deviation of the image histogram was calculated. The contrast measurement based on standard deviation correlates with human contrast perception better than other measurements independently from image histogram [53]. The values obtained from images acquired in SI-LSM or CLSM were then divided by the values calculated from LSM images of the same field of view, producing an adimensional ratio which is a good quantification of contrast enhancement. Neurites tracing and soma segmentation shown in Fig. 6(d) was performed using the filament editor and segmentation tools of Amira.

Acknowledgments

We thank Dr. Anna Letizia Allegra Mascaro and Dr. Francesco Vanzi for helpful discussion about the manuscript, Dr. Filippo Biamonte, Dr. Filippo Giorgi and Dr. Claudia Laperchia for assistance in perfusions, Mr. Riccardo Ballerini for mechanical assistance, Prof. Flavio Keller for providing us with L7-GFP mice. The research leading to these results has received funding from the European Union Seventh Framework Programme (FP7/2007-2013) under grant agreement n. 228334. This research project has been also supported by Human Frontier Science Program research grant (RGP0027/2009), and by the Italian Ministry for Education, University and Research in the framework of the Flagship Project NANOMAX. This research has been carried out in the framework of the research activities of ICON foundation supported by "Ente Cassa di Risparmio di Firenze".

Received 15 May 2012; revised 9 Jul 2012; accepted 9 Jul 2012; published 23 Aug 2012